Physics in Medicine & Biology

PAPER

Relative stopping power measurements and prosthesis artifacts reduction in proton CT

To cite this article: Carlo Civinini *et al* 2020 *Phys. Med. Biol.* **65** 225012

IOP Publishing Phys. Med. Biol. 65 (2020) 225012 https://doi.org/10.1088/1361-6560/abb0c8

Physics in Medicine & Biology

IPEM Institute of Physics and Engineering in Medicine

RECEIVED
30 April 2020

REVISED
14 August 2020

ACCEPTED FOR PUBLICATION
19 August 2020

PUBLISHED
12 November 2020

PAPER

Relative stopping power measurements and prosthesis artifacts reduction in proton CT

Carlo Civinini[1], Monica Scaringella[1], Mirko Brianzi[1], Matteo Intravaia[1,2,9], Nunzio Randazzo[3], Valeria Sipala[3,4], Marta Rovituso[5,10], Francesco Tommasino[5,6], Marco Schwarz[5,7] and Mara Bruzzi[1,8]

[1] Istituto Nazionale di Fisica Nucleare sezione di Firenze, via G. Sansone 1, Sesto Fiorentino (FI), Italy
[2] Dipartimento di Scienze dell'Informazione, Università degli Studi di Firenze, via S.Marta 3, Firenze, Italy
[3] Istituto Nazionale di Fisica Nucleare sezione di Catania, via S. Sofia 64, Catania, Italy
[4] Dipartimento di Chimica e Farmacia, Università degli Studi di Sassari, via Vienna 2, Sassari, Italy
[5] Istituto Nazionale di Fisica Nucleare TIFPA, via Sommarive, 14, Povo (TN), Italy
[6] Dipartimento di Fisica, Università di Trento, via Sommarive 14, Povo (TN), Italy
[7] Agenzia Provinciale per i Servizi Sanitari, via Al Desert 14, (TN), Italy
[8] Dipartimento di Fisica e Astronomia, Università degli Studi di Firenze, via G. Sansone 1, Sesto Fiorentino (FI), Italy
[9] Current address: Dipartimento di Ingegneria dell'Informazione e Scienze Matematiche, Università di Siena, Italy
[10] Current address: Holland Proton Therapy Center (HollandPTC), Delft, Holland

E-mail: carlo.civinini@fi.infn.it

Keywords: hadron therapy, proton tomography, stopping power, algebraic reconstruction techniques, metallic prosthesis

Abstract

We present a set-up for proton computed tomography (pCT), composed of a microstrip silicon tracker and a YAG:Ce calorimeter, able to directly measure the relative stopping power (RSP) maps to be used in hadron therapy. The system, tested with an electron density phantom at the Trento proton Therapy Center, is able to correlate measured and expected RSP with discrepancies of the order of 1% or less. Furthermore, pCT tomographies of an anthropomorphous head phantom taken with our device, when compared with x-ray CT images of the same object, evidence a significant reduction of artifacts induced by titanium spinal bone prosthesis and tungsten dental filling.

1. Introduction

Hadron therapy irradiates the tumor volume by moving the proton/ion beam and modulating the particles' energy to correctly place the Bragg peak within the selected position, while sparing as much as possible the surrounding healthy tissues. To this purpose, Treatment Planning Systems calculate the particle kinetic energy of the therapeutic beam and its direction using the proton relative stopping power normalized to liquid water (RSP) 3D distribution in the region crossed by the beam. Presently, the RSP maps, are extracted from conventional x-rays CT (x-CT) images translating the photon attenuation coefficients (Hounsfield's units—HU) by appropriate conversion and calibration coefficients (Schneider *et al* 1996). This method introduces an uncertainty on the position of the Bragg peak in the patient which may significantly reduce the advantages offered by the high spatial selectivity of hadrons. It is common practice in hadron therapy to assume an uncertainty of about 3% in the estimated range, and to compensate for that in the planning phase via intended 'overshooting', thus leading to an increased volume of healthy tissue being irradiated (Paganetti 2012). A 'proton computed tomography' (pCT) system, which directly measures the 3D RSP maps using the same irradiation beam with a much reduced intensity and a sufficient kinetic energy to be used in 'transmission mode', can mitigate this source of error. Furthermore, pCT images can be of paramount importance when the therapeutic beam crosses regions where metal prostheses are implanted. In fact, high Z materials are responsible of the appearance of severe artifacts in the x-CT images (Giantsoudi *et al* 2017). In such regions the estimation of the RSP maps becomes difficult due to the mismeasurement of the HU values.

Prototype pCT systems have been recently designed and constructed (Coutrakon *et al* 2013, Sadrozinski *et al* 2016, Johnson *et al* 2016, Pettersen *et al* 2016, Esposito *et al* 2018). An extensive review of the potential advantages of pCT techniques for increasing accuracy in proton therapy can be found in (Johnson 2018).

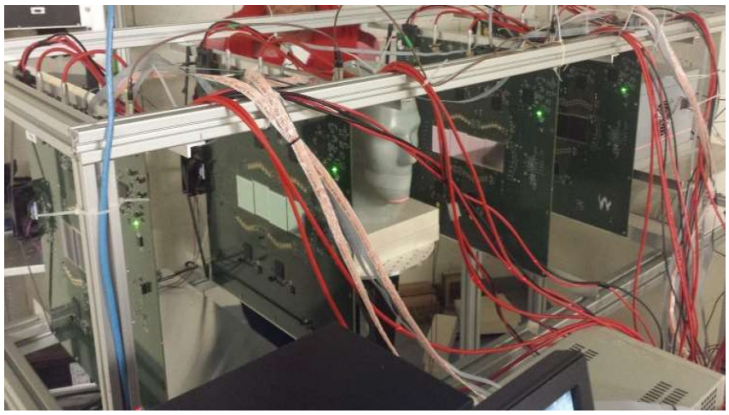

Figure 1. Picture of our pCT apparatus installed at the 'Trento Proton Therapy Center' experimental beam line. The proton beam enters the apparatus from the left. The tracker planes (green boards) and the calorimeter (grey box) are visible together with the anthropomorphous head phantom.

In the present work, we describe the results obtained with a pre-clinical pCT system quantifying these advantages in terms of accuracy in RSP measurement and artifact reduction.

Our pCT system is based on a silicon microstrip tracker and a Cerium-doped Yttrium Aluminum Garnet (YAG:Ce) scintillating calorimeter, with a 5×20 cm^2 field of view. It has been developed starting from a former prototype of smaller active area (Vanzi *et al* 2013, Civinini *et al* 2013, 2016, 2017, Scaringella *et al* 2013, 2014, Sipala *et al* 2015, Bruzzi *et al* 2017). We present results of the experimental tests carried out at the Trento Proton Therapy Center (APSS, Azienda Provinciale per i Servizi Sanitari, Trento, Italy) with this apparatus and two test objects (phantoms). One of these phantoms, shows that pCT can indeed obtain a reliable correlation between expected and measured RSPs. The other, an anthropomorphous head phantom, is used to investigate the potential of pCT in improving tomographic imaging as a consequence of the reduced impact of the artifacts induced by metallic prostheses, against x-CT.

2. Experimental procedures

The main difficulty encountered to increase accuracy with pCT is multiple coulomb scattering (MCS). In fact, with typical targets as thick as 20 cm (water equivalent), a 200 MeV proton beam undergoes a root-mean-square (RMS) MCS angle distribution of about 30 mrad.

On a 10 cm-distant plane, this brings the projected displacement distribution up to a 3 mm, or even higher, RMS. Therefore, simple proton projection radiographies cannot be used to extract the RSP map with a good precision.

The pCT solution to this problem is based on reconstructing the most likely path (MLP) of each proton crossing the object under test. In a pCT apparatus, the MLP is determined by sampling each proton trajectory both up- and down-stream the target, thus reconstructing two segments (Williams 2004). In this way, the maximum value of the one sigma error envelope on a transverse coordinate of the MLP of, for example, a 200 MeV energy proton in 20 cm of water, is about 0.5 mm (Schulte *et al* 2008). Each single-event information in a pCT is composed of the proton MLP estimated using the measurement coming from the tracker, and the proton energy loss measured by the calorimeter. A complete data-set needs measurements taken by rotating the phantom at many different angles. Then, algebraic reconstruction techniques (ART) (Li *et al* 2006), or alternative methods based on filtered backprojections (Rit *et al* 2013, Poludniowski *et al* 2014), are used to reconstruct the 3D RSP maps. In this section we will discuss in detail the main characteristics of our pCT system, the phantom and the proton beam used.

2.1. pCT apparatus

Figure 1 shows a picture of the complete apparatus mounted on the 'Trento Proton Therapy Center' experimental beam line while its simplified scheme is shown in figure 2.

The tracker is composed of four planes, each able to measure the 3D coordinates of the proton impact point to be used by the MLP algorithm to reconstruct the proton trajectory. A tracker plane is made by a single printed circuit board hosting the silicon microstrip sensors, the front-end and the digital read-out electronics. The silicon microstrip sensors are glued onto a rectangular aperture (20.3×4.9 cm^2) at the center of the board: four with the strips vertical, measuring the x coordinate (x-side) and four with strips horizontal, measuring the y coordinate (y-side). The two units are glued on the two sides of the board with

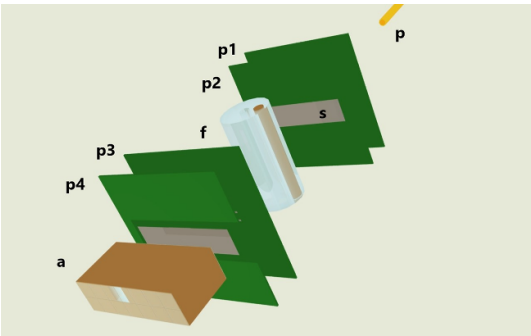

Figure 2. Simplified scheme of the pCT apparatus. (a) Calorimeter, f) phantom, s) silicon microstrip sensors, p1–p4) tracker planes, p) beam pipe.

the sensors mounted one next to the other with a small overlap to guarantee hermeticity. Each strip of an *x*-side sensor is connected to a front-end chip channel while two strips of the *y*-side sensors are daisy chained and readout by a single channel. In that way four groups, made up of eight front-end chips each, readout the *x*-side while two groups are used for the *y*-side. The strips are connected to the front-end electronics through a pitch-adapter directly designed on the printed circuit board.

The single-sided silicon microstrip sensors are of p-on-n type, with 256 strips at a pitch of 200 μm, a 5.1×5.1 cm^2 sensitive area and a thickness of 320 μm. The sensors have full depletion voltages around 85 V and an average bias current density at depletion of 2.5 nA cm^{-2}. The tracker front-end application-specific integrated circuit (Sipala *et al* 2017) is a VLSI device, developed by our collaboration, consisting of 32 channels and equipped with a charge amplifier, a shaper and a comparator producing a binary output by comparison with a threshold. They are connected to the data acquisition control system through an I2C line used to download the threshold values of each channel. The 32 digital output lines of the chip are connected to an FPGA (Xilinx, Spartan 6) which serves the group of 8 chips connected to a sensor. The six FPGAs of a tracker plane (four on the *x*-side and two on the *y*-side) are programmed to continuously sample the digital inputs from the front-end chips at 50 MHz keeping the information on a 128 cells deep circular buffer. After receiving a trigger signal from the calorimeter electronics the FPGA scans in parallel the 256 inputs, using also pre-trigger samples, to find active strips. Only for them, information concerning initial time with respect to the trigger, signal duration and strip number are assembled within the six first level FPGAs and then moved to a second level FPGA on the same plane, using eight line buses each running at an aggregate 1.6 Gb s^{-1} transfer rate. The second level FPGA, after event synchronism control, assembles the fired strips in each of the six groups attaching to the data structure the event number and its time. After data building, the information is transferred to a third level FPGA (Virtex 6, Xilinx), for the final event assembly of the four tracker planes together with the calorimeter data.

During the test described in this paper the instantaneous data acquisition rate was 80 kHz while the average was reduced to 15 kHz due to the dead time introduced by the data transfer to the main acquisition PC. This leads to a total time to acquire a full tomographic data-set of about two hours. The data transfer dead time issue has been addressed and solved after the data taking described in this paper.

While the pCT devices described in (Pettersen *et al* 2016, Esposito *et al* 2018) use a range counter for the determination of the residual range of the proton, the system described in this article uses a YAG:Ce scintillation calorimeter to measure the particles' residual energy. This calorimeter is made by a 2×7 scintillating crystal matrix and it is placed just after the fourth tracker plane. The 'pixelated' shape of the calorimeter helps to withstand higher beam rate reducing the single channel occupancy. Each crystal has a 3×3 cm^2 section and a 10 cm length and is readout by a silicon photodiode (1.8×1.8 cm^2 area) which is insensitive to the stray magnetic field commonly present at the end of a transmission beam line. The YAG:Ce crystal has been selected both for its short light decay constant (70 ns) and an emitting light spectrum well matching the photodiode sensitivity range. The 14 analog signals are amplified, shaped and then digitally converted at 5 MHz and 14 bits. Each event contains 32 samples per crystal and it is transferred to the main data acquisition unit.

To calibrate the calorimeter we took data, without any phantom installed between the tracker planes, at six different energies in the range 70–211 MeV, with about 10^7 events per energy point. To correct for crystal inhomogeneties we subdivided each calorimeter crystals in 10×10 cells with front face dimensions of 3×3mm^2 and, with the help of the tracker which extrapolates the tracks to the calorimeter, we reconstructed the energy response of each cell. With this procedure a set of 1400 calibration curves has been implemented.

Table 1. Electron density phantom (CIRS 062M) material density, expected SP and RSP values for 180 MeV protons, and MLIC-measured RSP.

Material	Density g/cm^3	Geant4 SP MeV/cm	Geant4 RSP	MLIC-measured RSP
Lung (inhale)	0.205	0.979	0.204	0.26
Lung (exhale)	0.507	2.449	0.511	0.54
Adipose	0.96	4.655	0.971	0.96
Breast	0.99	4.775	0.996	1.02
Distilled water	1	4.792	1	–
Plastic equiv. water	1.029	4.822	1.006	–
Muscle	1.06	5.076	1.059	1.06
Liver	1.07	5.133	1.071	1.06
Bone (trabecular)	1.16	5.357	1.118	1.40
Bone (dense)	1.53	6.767	1.412	1.12

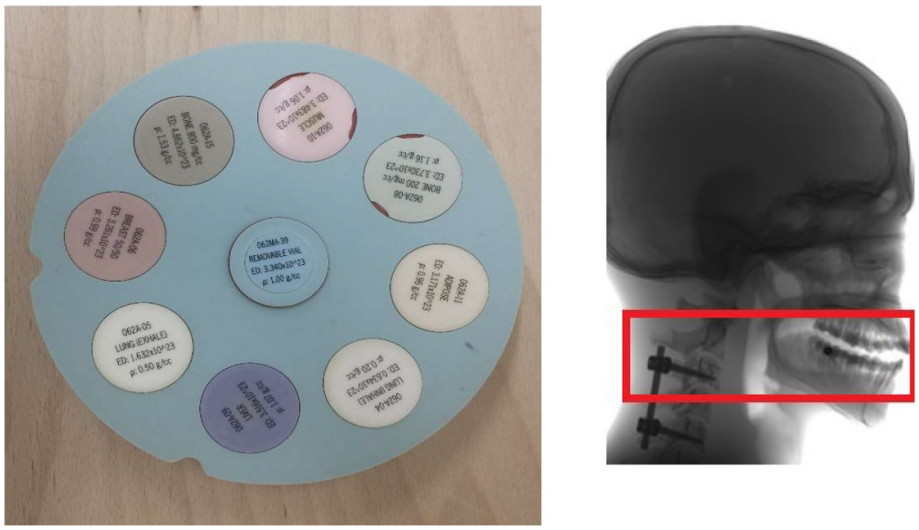

(a) (b)

Figure 3. (a) Picture of the electron density phantom with nine inserts of different tissue equivalent materials (see table 1). (b) X-ray radiography of the anthropomorphic average male head phantom: a tungsten dental filling and a titanium vertebra prosthesis are visible. The red box highlights the volume where the proton tomography has been performed.

Once calibrated the energy resolution of the pCT calorimeter has been measured to be 1.3% at 211 MeV with approximately the same absolute value of 2.6 MeV at the other energies in the range 70–211 MeV.

2.2. Test phantoms

Figure 3(a) shows the phantom used for the pCT RSP measurement (CIRS 062M, Electron Density—ED—phantom); this is an 18 cm diameter cylinder, 5 cm height, made of water equivalent plastic (Plastic Water®-LR). The phantom contains nine exchangeable inserts made of different tissue substitutes (see table 1). The central insert contains a vial filled with distilled water. The mean value of the water SP measured in this vial is used as reference to compute the RPS of the various materials.

The water equivalent thickness (WET) values of some of the ED phantom inserts have been measured using a pencil beam and a multi-layer ionization chamber (MLIC, Giraffe, IBA) (Fellin *et al* 2017). To get the RSP values reported in table 1, the WETs have been divided by the insert's axial length (50 mm). Since the two lung inserts have their upper edges made of a denser reinforcement material, their WET measurements resulted in overestimated values and are therefore excluded from the comparison with the pCT measured RSP. Columns 3 and 4 of table 1 report the expected SP and RSP computed using Geant4 (Agostinelli *et al* 2003, Allison *et al* 2006, 2016). This calculation makes use of the elemental inserts' compositions (Gomà *et al* 2018), densities, mean excitation energies from ICRU 37 report (Berger *et al* 1984) applying the Bragg additivity rule. The mean excitation energy value for liquid water ($I_W = 78$ eV) recommended in (Recommended values for key data 2014) has been used.

We also studied an anthropomorphous average male head phantom (CIRS 731-HN) manufactured with tissue-equivalent materials, which mimic reference tissues within 1.5% for protons' RSP. Figure 3(b) shows its x-ray radiography.

Internal structures of the phantom include brain, bone with cortical and trabecular distinction, larynx, trachea, fully-open sinus cavities, nasal and mouth cavities, and teeth with distinct dentine, enamel and root structure.

Furthermore, a tungsten filling in a molar and a titanium prosthesis attached by two screws at C3 and C5 vertebra are present. These metal inserts are useful to study the possible artifacts generated by high density materials. The phantom is composed of four vertical sections with narrow gaps between them to allow the insertion of radiochromic films.

2.3. Experimental proton beam line

The Trento Proton Therapy Center experimental beam line has been extensively characterized in (Tommasino *et al* 2017). The nominal beam energies were determined during the commissioning on the machine (Ion Beam Applications IBA, Proteus 235 cyclotron). Specifically, the range was determined based on Bragg curve measurements performed in a water phantom positioned after the cyclotron energy degrader. Based on a procedure adopted in all IBA centers involving a multi-parametric fit, the range was then converted into primary beam energy.

The pCT apparatus has been installed with the first tracker plane at a distance of 363 cm from the beam pipe vacuum exit window. The distance between the first and the second tracker plane, as well as the one from the third and fourth, has been set to 30 cm. The space left free between the second and third plane, where the phantoms have been installed, was 50 cm.

A nominal proton kinetic energy of 211.2 MeV has been used during the full tomographic data taking. This corresponds to a measured proton energy at the iso-center (125 cm from the beam pipe exit window) of 210 MeV.

A 2.5 mm thick tantalum plate has been placed just after the pipe end to spread the beam in order to cover the full pCT field of view. The average proton energy loss inside the plate, 9.66 MeV, has been calculated by a Geant4 simulation and taken into account to evaluate the correct energy loss inside the phantom. The tantalum plate adds, in quadrature, 0.58 MeV (0.27%) to the original beam energy spread of 0.3% (Tommasino *et al* 2017). Since the calorimeter energy resolution is 1.3% the influence of this additional contribution is negligible.

3. Image reconstruction methods

To properly take into account the non-straight trajectory of the protons due to multiple scattering, the reconstruction of the pCT images was not performed using the Filtered Back Projection but rather implementing an ART algorithm (*Gordon et al 1970*).

3.1. Tomographic reconstruction equations

The proton SP map, $S(x,y,E)$, is defined as

$$-\mathrm{d}E = S(x,y,E)\,dl \tag{1}$$

where $-dE$ is the energy loss of a particle with energy E in a dl path at point x,y. Introducing the mass stopping power as $\frac{S}{\rho}(x,y,E) = \frac{S(x,y,E)}{\rho(x,y)}$, where $\rho(x,y)$ is the material density, (1) can be rewritten as

$$-\frac{S}{\rho}(x,y,E_0)\,dE = \frac{S}{\rho}(x,y,E_0)\,\frac{S}{\rho}(x,y,E)\,\rho(x,y)\,dl \tag{2}$$

Dividing (2) by the mass stopping power at energy E:

$$-\frac{\frac{S}{\rho}(x,y,E_0)}{\frac{S}{\rho}(x,y,E)}dE = S(x,y,E_0)\,dl,\ (3.3)\ -\frac{\frac{S}{\rho}(x,y,E_0)}{\frac{S}{\rho}(x,y,E)}dE = S(x,y,E_0)\,dl \tag{3}$$

E_0 being a reference energy at which the stopping power is calculated (e.g. 180 MeV for this analysis). At this energy the stopping power ratio of (3) does not depend too much (<6‰) on the material composition and could be replaced by the one measured for liquid water (Berger *et al* 2017):

$$-\left[\frac{S}{\rho}(H_2O)\right]_E^{E_0} dE = S(x,y,E_0)\,dl \tag{4}$$

where

$$\left[\frac{S}{\rho}(H_2O)\right]_E^{E_0} \cong \left[\frac{S}{\rho}(x,y)\right]_E^{E_0} = \frac{S}{\rho}(x,y,E_0)\,/\,\frac{S}{\rho}(x,y,E)\,. \tag{5}$$

Integrating along the proton path we obtain the tomographic equation:

$$-\int_{E_{in}}^{E_{out}}\left[\frac{S}{\rho}(H_2O)\right]_E^{E_0} dE = \int_{path} S(x,y,E_0)\,dl. \tag{6}$$

In (6), E_{in} and E_{out} are the energies of the proton entering and exiting the phantom; '*path*' is the best estimation of the proton trajectory inside the phantom as extracted using the MLP formalism (Williams 2004, Schulte *et al* 2008) from the tracker measurements. To properly build the trajectory inside the phantom material the two track segments were extrapolated to an approximate phantom border. The two interception points are then connected using the MLP algorithm. This border is a cylinder embedding the phantoms' material.

A discretization of (6) can be done by dividing the phantom into a set of N pixels. For M protons the following set of linear equations can be written:

$$p_i \equiv -\int_{E_{in}}^{E_{out}}\left[\frac{S}{\rho}(H_2O)\right]_E^{E_0} dE = \sum_{j=1}^{N} w_{ij} S_j(E_0)$$
$$i = 1,\ldots,M \tag{7}$$

where p_i is measured using the calorimeter information for i-th proton and w_{ij} is the trajectory length of i-th proton in the pixel j. The w_{ij} coefficients are experimentally evaluated dividing the i-th proton MLP in a large number of equal length segments and counting how many of them lie within pixel j.

The tomographic reconstruction problem (Wang *et al* 2010) is then reduced to solve for $S_j(E_0)$, the stopping power value at pixel j for energy E_0, the linear system (7).

3.2. Iterative algebraic reconstruction algorithms

Large linear equation systems like (7) are usually solved by means of iterative algebraic techniques (Gordon *et al* 1970). These methods start from an arbitrary initial image, which could be a totally 'blank' picture or an approximation of the phantom obtained with less precise but faster methods, and iteratively project this image onto each of the equation (hyperplanes) (7) obtaining a sequence of points in the N-dimensional space of the unknowns which converges to the solution.

The system (7) typically has more equations than unknowns. This, together with the uncertainties introduced by the finite apparatus resolutions, implies that an image which exactly satisfies all conditions (7) does not exist. Nonetheless, the sequence obtained iteratively projecting the image onto the hyperplanes, converges to an N-dimensional volume where the hyperplane intersection density is high and not too far from the real image.

The ART iterative formula used to solve (7) is defined as

$$S^{k+1} = S^k + \lambda_k \frac{p_{i(k)} - w^{i(k)}|S^k}{{w^{i(k)}}^2} w^{i(k)} \tag{8}$$

where $i(k) = (k \bmod M) + 1$ is a cyclic sequence on the event number (e.g. for three events $i(k) \rightarrow$ *1,2,3,1,2,3,…*), S^k is the N-dimensional image vector at iteration k, $w^{i(k)}$ the $i(k)$th track length in each pixel and $p_{i(k)}$ is the stopping power integral of the $i(k)$th proton (7). The relaxing factor λ_k could be a constant or a sequence converging to zero. The algorithm starts with an image S_0 and stops if the quantity $\Delta = S^{i(k+1)} - S^{i(k)}$ is below a threshold. In (8) a|b is the scalar product of the two vectors, while $\|a\|$ is the Euclidean norm.

To reduce the 'salt-pepper' noise introduced by the resolution-induced internal inconsistency of (7), a variation of ART has been introduced. This technique (simultaneous algebraic reconstruction technique, SART (Andersen and Kak 1984)) still uses the projection of the image as in (8) but updates S^k using an average over the full data set of the projections (9):

$$S^{k+1} = S^k + \frac{\lambda_k}{M}\sum_{i=1}^{M} \frac{p_i - w^i|S^k}{{w^i}^2} w^i. \tag{9}$$

SART has a fundamental computational advantage with respect to ART: since the correction to the image is done at the end of a cycle over the total number of events, it is easily parallelizable. A drawback is that the average could be a small number (M is large), so increasing the convergence time.

To overcome this problem, the data set is divided into a number of blocks and the average is not done on the event number but on the number of tracks intercepting a particular pixel (Censor *et al* 2008):

$$S_j^{k+1} = S_j^k + \frac{\lambda_k}{T_j^{t(k)}} \sum_{i \in B_{t(k)}} \frac{p_i - w^i | S^k}{w^{i2}} w_j^i. \tag{10}$$

In (10), the total data set I has been divided into T blocks B_t such that $I = \bigcup_{t=1}^{T} B_t$, the iterations are done over a cyclic sequence of blocks $t(k) = (k \; mod \; T) + 1$, $T_j^{t(k)}$ being the number of tracks in block $B_{t(k)}$ intersecting the pixel j.

3.3. Image reconstruction

The iterative algebraic technique used to reconstruct the pCT images shown in this paper is the SART algorithm with its variant described in equation (10) with four blocks.

The ED phantom has been reconstructed in a cylindrical volume with the axis coincident with the rotational one. The volume has been subdivided into elementary voxels $0.600 \times 0.600 \times 1.650$ mm^3 each: the 600 μm sizes are within the plane orthogonal to the rotation axis, while the latter one is the tomography slice thickness. The total number of voxels is $512 \times 512 \times 32$. The pCT image of the anthropomorphous head phantom has been reconstructed in the same cylindrical volume where the vertical number of slices have been doubled halving the voxel volume ($0.600 \times 0.600 \times 0.825$ mm^3).

The total number of events for the ED and anthropomorphous head phantoms image data-sets are 10^8 (10^4 mm^{-2}) and 1.2×10^8 (1.2×10^4 mm^{-2}) respectively. The calculated doses corresponding to these numbers of events are 0.9 mGy (ED) and 1.1 mGy (anthropomorphous head).

The fraction of events used by the reconstruction algorithm is about 40% of the ones actually acquired. Part of this inefficiency depends on the beam rate which introduces pileup protons. For the future runs the analysis software will be upgraded to deal with multitrack events.

The analysis cuts were organized as follows: first we select events with one track, then the angle between the two track segments is requested to be less than three times the multiple scattering distribution's sigma. Since the calorimeter measurements when the proton has a nuclear interaction in the crystals is underestimated, we remove this kind of events requesting a measured energy compatible with its expected energy loss.

The images evolution as function of the reconstruction iteration step has been checked looking at the variation of the mean RSP values in different regions of interest (ROIs) of the ED phantom. At the ED phantom stopping iteration (n. 75) the maximum RSP variation with respect to the previous step is very small (less than 5×10^{-5}) and constantly decreasing.

To calculate the RSP of the material of each ED phantom inserts, ten ROIs have been defined and the SP distribution in each ROI has been fitted with a Gaussian to get the mean and sigma values. The RSP of each material is then calculated as the material's fitted mean value divided by the same quantity calculated for the liquid water. The liquid water ROI, due to the particular shape of the vial, is a 7.8 mm radius cylinder, coaxial with the vial, spanning in height from tomography slice 7 to 16 (14.85 mm); the plastic water ROI is a cylindrical shell with an inner radius of 24 mm and an external radius of 30 mm covering all the slices. The other materials ROIs are cylinders, coaxial with the inserts, with a radius of 10.2 mm spanning from slice 6 to 27 (34.65 mm).

The water vial SP measurement is used to calibrate the full pCT system correcting for possible errors in the calorimeter absolute energy determination. This water vial calibration will be periodically done, not necessarily together with the tomography of the object under test.

4. Results and discussion

4.1. Electron density phantom

Figure 4 shows the central slice of the reconstructed ED phantom image. This picture clearly shows the presence of all the different material inserts, besides the two indents at perimeter. Indeed, we can recognize the presence of air gaps around some of the inserts (breast, liquid water and adipose). As expected, the higher contrast is obtained for lung and bone which are characterized by a SP quite different from that of the plastic equivalent water matrix (see table 1).

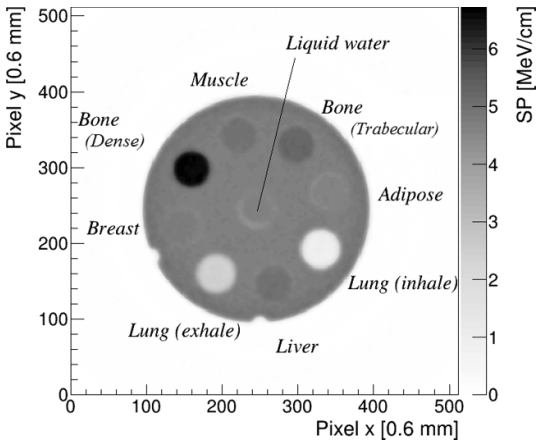

Figure 4. The central slice (1.65 mm thick) reconstructed image at iteration n. 75 of the ED phantom tomography. The grey levels are proportional to the absolute SP calculated for $E_0 = 180$ MeV.

Table 2. pCT measured RSPs (mean and sigma) and its percentage difference between the MLIC-measured and Geant4 expected values.

Material	pCT-measured RSP (mean)	pCT-measured RSP (sigma)	pCT-MLIC RSP relative difference [%]	pCT-Geant4 RSP relative difference [%]
Lung (inhale)	0.192	0.009	−35.6	−6.53
Lung (exhale)	0.526	0.009	−3.15	2.40
Adipose	0.976	0.008	1.62	0.47
Breast	1.017	0.009	−0.26	2.06
Distilled water	1	0.006	–	–
Plastic equiv. water	1.006	0.006	–	−0.05
Muscle	1.065	0.008	0.44	0.52
Liver	1.070	0.010	0.97	−0.06
Bone (trabecular)	1.118	0.008	−0.20	−0.003
Bone (dense)	1.414	0.009	0.96	0.11

A possible factor influencing the spatial resolution of the image is the scattering that protons undergo when passing through the silicon microstrip sensors. This effect is amplified by the distance between the phantom and the tracker planes.

For mechanical reasons, this version of the pCT system has been assembled with a distance between the second and third tracker plane of 50 cm. To increase the spatial resolution of the pCT images this critical distance will be reduced in the future.

To quantify the ability of the pCT system to reconstruct the correct RSP, these values have been evaluated from the ED phantom tomography and compared with the expected ones reported in table 1.

In table 2 the pCT measured mean and sigma values of the Gaussian fit to the RSP distribution in the ROI are reported together with the relative difference with respect to the MLIC-measured and Geant4 expected RSP values. Excluding the two lung inserts for the reasons explained in sect. 2.2, the maximum deviation between the pCT- and MLIC-measured RSP is about 1.6%. The mean absolute percentage error (MAPE) for the pCT/MLIC is 0.74% while for the pCT/Geant4, for the same materials, is 0.54%. These values are very close to the pCT and dual energy x-CT measurements reported in (Dedes *et al* 2019).

Figure 5 shows the correlation between pCT measured and Geant4 expected RSPs. Here the systematic error on the expected values has been assumed to be the difference between the Geant4 predicted value for liquid water and the corresponding one obtained from the NIST table (Berger *et al* 2017). The error on the pCT measured RSP is the standard deviation calculated with the Gaussian fit. The inset in the figure 5 is a detailed view of the region close to the water RSP value, corresponding to the soft-tissue range.

Data in figure 5 have been fitted with a linear regression: $y = p_1\, x + p_0$. A very good correlation is evidenced by the slope and intercept values, compatible respectively with 1 and 0 within their uncertainties. The quality of the fit is excellent, as evidenced by the χ^2 value.

4.2. Anthropomorphous head phantom

All the following images have been processed using ImageJ (Rueden *et al* 2017) starting from the reconstructed RSP values.

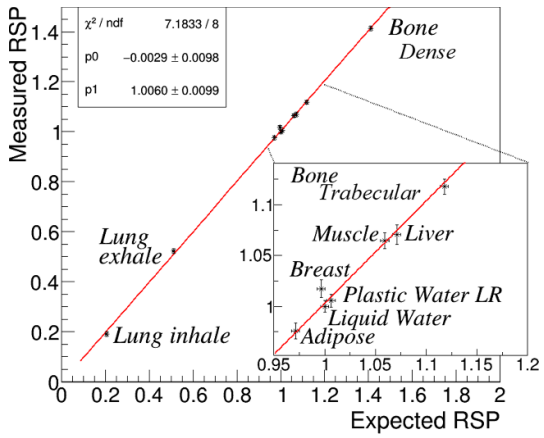

Figure 5. Comparison between pCT measured and Geant4 expected RSP values of the materials within the ED phantom. Data fitted to a linear function. Inset: detailed view of the region close to RSP = 1.

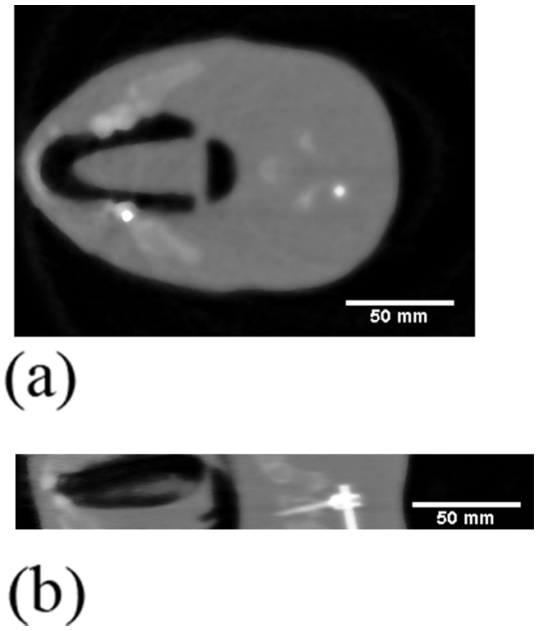

Figure 6. Anthropomorphous head phantom pCT image (iteration n. 62): (a) horizontal slice of the dental filling region. (b) Vertical slice in a plane containing the titanium vertebral prosthesis.

Figure 6(a) shows a pCT horizontal slice of the phantom at the level of the tungsten dental filling. Figure 6(b) shows a pCT vertical slice of the phantom in a plane which contains the titanium prosthesis. As it can be seen, the anatomical details are clearly visible and no artifacts are present in both images. We can clearly distinguish the larynx and the mouth empty spaces together with the tongue and the lower dental arc. Two bright spots are visible in figure 6(a): the tungsten dental filling and a section of the titanium vertebra prosthesis. This latter is visible, close to the spine, in figure 6(b). Here, we can also clearly distinguish the screw inserted into the vertebra.

4.3. Metal artifacts analysis

Results described in section 4.1 show that our pCT system is able to get a very accurate and direct measurement of the RSP values of (surrogate) biological tissues. This is in itself an outcome putting into evidence the importance of pCT as a tool to significantly improve the accuracy in hadron therapy treatments against the standard x-CT.

Going further, in this work we investigated the effect of metallic prostheses on the image quality of pCT vs x-CT. To this purpose, figure 7 shows the x-CT image of the anthropomorphous head phantom shown in figure 6(a) (same slice). The x-CT tomographies shown in this section have been acquired using a Philips scanner (Brilliance Big Bore Philips Medical Systems). The acquisition parameters were as follows: voltage

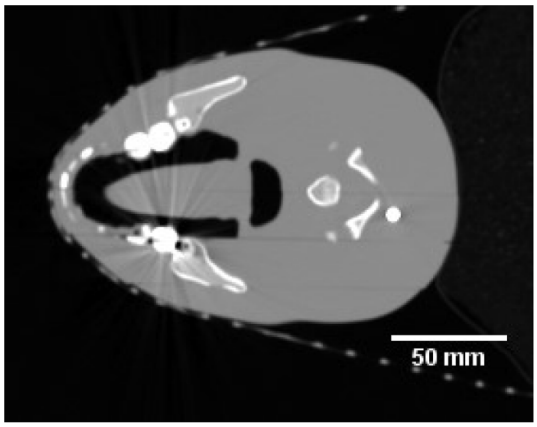

Figure 7. Horizontal slice of the anthropomorphous phantom head x-CT tomography.

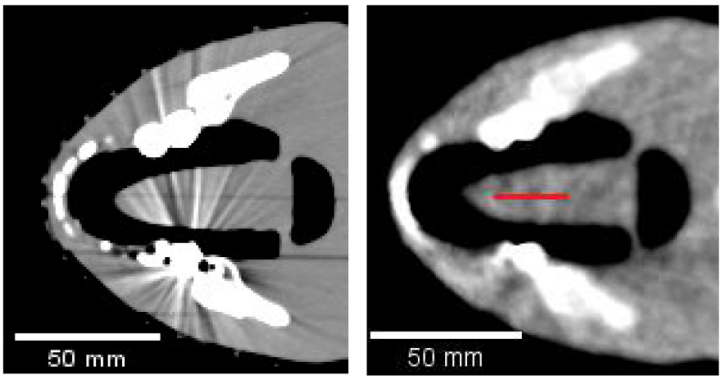

Figure 8. Close-up view, with enhanced contrast, of the tungsten dental filling region: (a) x-CT shown in figure 7; (b) pCT shown in figure 6(a). Red line indicates the ROIs used to quantify the standard deviation of the HU and RSP values.

120 kVp, exposure 450 mAs, slice thickness 1 mm, collimation 16×0.75 mm^2, scan field of view diameter 600 mm, reconstruction non optimized for artifact reduction with filter type Brain Standard (UB) and voxel dimensions $0.809 \times 0.809 \times 1.230$ mm^3.

Evident artifacts produced in the x-CT image by the high density/high Z values of the tungsten and titanium materials are clearly visible. Conversely, in figure 6(a) the metal induced artifacts are much less evident. Nonetheless, the image here appears much more blurred, due to the lower spatial resolution of pCT, an obvious effect of MCS, so it is not straightforward to draw stronger conclusions from this qualitative evidence.

To visually enhance and compare the two images in the regions close to the metal inserts, we show, in figures 8(a) and (b) respectively for the x-CT and pCT horizontal slices, zoomed regions close to the dental tungsten filling; same for titanium prosthesis is shown in figures 9(a) and (b).

Here the full grey scale corresponds to a same 40% range around distilled water value ($800 \leq$ HU ≤ 1200 and $0.8 \leq$ RSP ≤ 1.2). Figures 8(a) and 9(a) clearly show artifacts induced by the prosthesis in x-CT. These artifacts appear much attenuated in pCT images of figures 8(b) and 9(b).

A quantitative comparison between pCT and x-CT tomographic images in the presence of the two metallic objects has been done by calculating the standard deviation of the RSP and HU values in sets of ROIs close to tungsten and titanium prostheses, where the material is expected to be uniform.

The two sets of ROIs are one pixel wide, 32.3 mm long, and distant 11.3 mm and 20.2 mm respectively from tungsten and titanium prostheses. The tungsten set of ROIs, one per slice, span 11 mm in the direction orthogonal to figure 8 plane, while the titanium ones 33 mm in the direction orthogonal to figure 9 plane. They are shown in figures 8(b) and 9(b) as red lines.

Figures 10 and 11 show the standard deviation of the RSP, normalized to the average value, in both sets of ROIs, as a function of the slice coordinate. The origin of the slice coordinate has been set conventionally to zero for the slice of maximum x-CT standard deviation value (named tungsten and titanium plane in figures

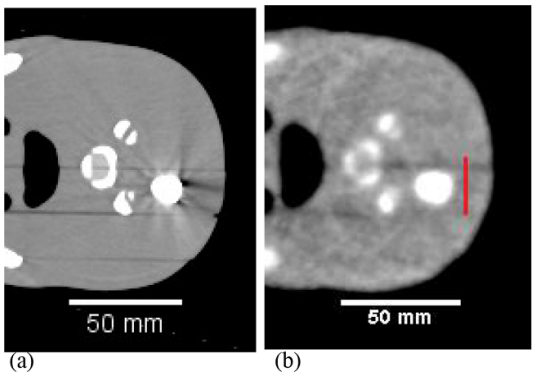

Figure 9. Close-up view, with enhanced contrast, of the titanium prosthesis region: (a) x-CT shown in figure 7; (b) pCT shown in figure 6(a). Red line indicates the ROIs used to quantify the standard deviation of the HU and RSP values.

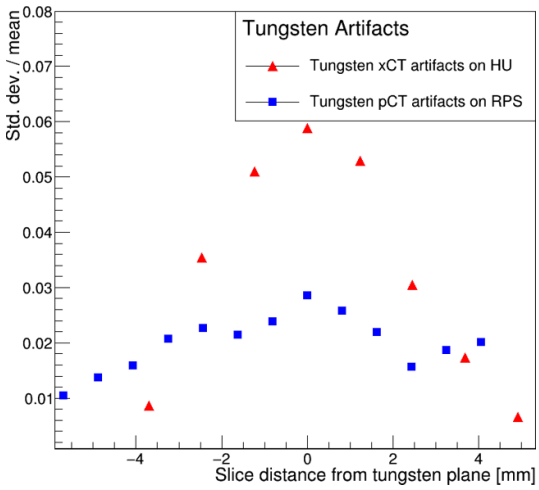

Figure 10. RSP (pCT, blue square) and HU (x-CT, red triangle) standard deviation, normalized to the RSP or HU average value, calculated within the ROIs close to the tungsten dental filling shown in figure 8(b). The abscissa is the slice distance from the plane of maximum x-CT standard deviation value.

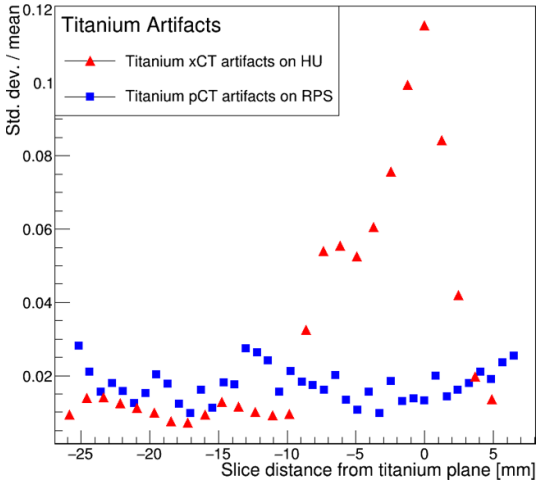

Figure 11. RSP (pCT, blue square) and HU (x-CT, red triangle) standard deviation, normalized to the RSP or HU average value, calculated within the ROI close to the titanium prosthesis shown in figure 9(b). The abscissa is the slice distance from the plane of maximum x-CT standard deviation value.

10 and 11). In the x-CT ROIs close to the tungsten and titanium implants, fluctuations are up to 6% and 12%, respectively, while these artifacts are reduced to a 2%–3% in pCT images in the same regions.

In the slices away from the artifacts, the RSP standard deviation in x-CT is lower than in pCT images (~1% against ~2%). In the pCT image, the standard deviation is higher than the (0.6–1.0)% range obtained in the ED phantom (see table 2); this, as observed in (Dickmann *et al* 2019), is probably due to the heterogeneity of the head phantom.

5. Conclusions

A pCT system, composed of a microstrip silicon tracker and a YAG:Ce calorimeter, has been manufactured and tested at the Trento proton Therapy Center by our collaboration. Measurements have been carried out using a 211 MeV proton beam with a certified electron density phantom. Proton tomography images obtained by customized iterative algebraic reconstruction algorithms show that our system is able to correlate measured and expected RSP with discrepancies of the order of 1% or less. Although not yet confirmed by measurements on biological samples, such a precise direct determination of RSP maps demonstrates that our pCT system could be indeed quite beneficial for improving quality assurance protocols in particle therapy facilities. Further, a main open issue in hadron therapy is how to handle artifacts in x-CT images due to the presence of metal prostheses. We therefore performed a first quantitative comparison of artifacts produced by metal prostheses in x-CT and pCT. Tests have been carried out with our device using an anthropomorphous head phantom carrying a titanium spinal bone prosthesis and a tungsten dental filling. Reconstructed pCT images evidence a significant reduction of artifacts in the proximity of prostheses against those found in x-CT ones. Standard deviations normalized to mean values up to 12% and 6% have been found for x-CT in ROIs distant about 2 cm from titanium spinal bone and 1 cm from tungsten dental filling respectively. In same ROIs of pCT images, standard deviations are reduced to about 2%–3%. Better immunity of pCT to prostheses related artifacts is probably due to the fact that the protons energy loss in metal is more correctly evaluated than the absorption of x-rays in high Z materials. This further experimental result evidences the potential benefit of using pCT as a tool to reduce treatment related uncertainties, eventually allowing more conformal irradiation.

Acknowledgments

This work has been performed in the framework of PRIMA-RDH-IRPT_PP experiments funded by INFN-CSN5 and MIUR, Italy, and partially financed by 'Fondazione CR Firenze' (Grant No. 2018.1174). The authors wish to thank Roberto Righetto (APSS, Trento) for the MLIC measurements of the ED phantom inserts.

ORCID iDs

Carlo Civinini https://orcid.org/0000-0002-4952-3799
Francesco Tommasino https://orcid.org/0000-0002-8684-9261
Marco Schwarz https://orcid.org/0000-0001-6964-7732

References

Agostinelli S *et al* 2003 GEANT4: a simulation toolkit *Nucl. Instrum. Methods Phys. Res.* A **506** 250–303
Allison J *et al* 2006 Geant4 developments and applications *IEEE Trans. Nucl. Sci.* **53** 270–8
Allison J *et al* 2016 Recent developments in GEANT4 *Nucl. Instrum. Methods Phys. Res.* A **835** 186–225
Andersen A H and Kak A C 1984 Simultaneous Algebraic Reconstruction Technique (SART): a superior implementation of the ART algorithm *Ultrason. Imaging* **6** 8–94
Berger M J, Coursey J S, Zucker M A and Chang J 2017 Stopping-power & range tables for electrons, protons, and helium ions *NIST Stand. Ref. Database* **124**
Berger M J, Inokuti M, Anderson H H, Bichsel H, Dennis J A, Powers D, Seltzer S M and Turner J E 1984 ICRU report 37 *J. Int. Comm. Radiat. Units Meas.* **os19** 15–31
Bruzzi M *et al* 2017 Proton computed tomography images with algebraic reconstruction *Nucl. Instrum. Methods Phys. Res.* A **845** 652–5
Censor Y, Elfving T, Herman G T and Nikazad T 2008 On diagonally relaxed orthogonal projection methods *SIAM J. Sci. Comput.* **30** 473–504
Civinini C *et al* 2013 Recent results on the development of a proton computed tomography system *Nucl. Instrum. Methods Phys. Res.* A **730** 573–6
Civinini C *et al* 2016 Proof-of-Principle results of proton computed tomography 2016 *IEEE Nuclear Science Symp., Medical Imaging Conf. and Room-Temperature Semiconductor Detector Workshop (NSS/MIC/RTSD) (Strasbourg)* pp 1–6
Civinini C *et al* 2017 Proton computed tomography: iterative image reconstruction and dose evaluation *JINST* **12** C01034
Coutrakon G, Bashkirov V, Hurley F, Johnson R, Rykalin V, Sadrozinski H and Schulte R 2013 Design and construction of the 1st proton CT scanner *AIP Conf. Proc.* **1525** 327

Dedes G et al 2019 Experimental comparison of proton CT and dual energy x-ray CT for relative stopping power estimation in proton therapy Phys. Med. Biol. 64 165002
Dickmann J et al 2019 Prediction of image noise contributions in proton computed tomography and comparison to measurements Phys. Med. Biol. 64 145016
Esposito M et al 2018 PRaVDA: the first solid-state system for proton computed tomography Phys. Med. 55 149–54
Fellin F, Righetto R, Fava G, Trevisan D, Amelio D and Farace P 2017 Water equivalent thickness of immobilization devices in proton therapy planning—modelling at treatment planning and validation by measurements with a multi-layer ionization chamber Phys. Med. 35 31–38
Giantsoudi D et al 2017 Metal artifacts in computed tomography for radiation therapy planning: dosimetric effects and impact of metal artifact reduction Phys. Med. Biol. 62 R49–R80
Gomà C, Almeida I P and Verhaegen F 2018 Revisiting the single-energy CT calibration for proton therapy treatment planning: a critical look at the stoichiometric method Phys. Med. Biol. 63 235011
Gordon R, Bender R and Herman G T 1970 Algebraic reconstruction techniques (ART) for three-dimensional electron microscopy and x-ray photography J. Theor. Biol. 29 471–81
Johnson R P et al 2016 A fast experimental scanner for proton CT: technical performance and first experience with phantom scans IEEE Trans. Nucl. Sci. 63 52–60
Johnson R P 2018 Review of medical radiography and tomography with proton beams Rep. Prog. Phys. 81 016701
Li T, Liang Z, Singanallur J V, Satogata T J, Williams D C and Schulte R W 2006 Reconstruction for proton computed tomography by tracing proton trajectories—A Monte Carlo study Med. Phys. 33 699–706
Paganetti H 2012 Range uncertainties in proton therapy and the role of Monte Carlo simulations Phys. Med. Biol. 57 R99–R117
Pettersen H E S et al 2016 Proton tracking in a high-granularity digital tracking calorimeter for proton CT purposes Nucl. Instrum. Methods Phys. Res. A 860 51–61
Poludniowski G, Allinson N M and Evans P M 2014 Proton computed tomography reconstruction using a backprojection-then-filtering approach Phys. Med. Biol. 59 7905–18
Recommended values for key data 2014 No 1 Report 90 J. ICRU 14 31–48
Rit S, Dedes G, Freud N, Sarrut D and Létang J M 2013 Filtered backprojection proton CT reconstruction along most likely paths Med. Phys. 40 031103
Rueden C T et al 2017 ImageJ2: ImageJ for the next generation of scientific image data BMC Bioinform. 18 529
Sadrozinski H F-W et al 2016 Operation of the preclinical head scanner for proton CT Nucl. Instrum. Methods Phys. Res. A 831 394–9
Scaringella M et al 2013 The PRIMA (PRoton IMAging) collaboration: development of a proton Computed Tomography apparatus Nucl. Instrum. Methods Phys. Res. A 730 178–83
Scaringella M et al 2014 A proton Computed Tomography based medical imaging system JINST 9 C 12009
Schneider U, Pedroni E and Lomax A 1996 The calibration of CT Hounsfield units for radiotherapy treatment planning Phys. Med. Biol. 41 111–24
Schulte R W, Penfold S N, Tafas J T and Schubert K E 2008 A maximum likelihood proton path formalism for application in proton computed tomography Med. Phys. 35 4849–56
Sipala V et al 2015 Design and characterisation of a YAG(Ce) calorimeter for proton computed tomography application JINST 10 C 03014
Sipala V et al 2017 A binary readout chip for silicon microstrip detector in proton imaging application JINST 12 C01030
Tommasino F et al 2017 Proton beam characterization in the experimental room of the Trento Proton Therapy facility Nucl. Instrum. Methods Phys. Res. A 869 15–20
Vanzi E et al 2013 The PRIMA collaboration: preliminary results in FBP reconstruction of pCT data Nucl. Instrum. Methods Phys. Res. A 730 184–90
Wang D, Mackie T R and Tomé W A 2010 On the use of a proton path probability map for proton computed tomography reconstruction Med. Phys. 37 4138–45
Williams D C 2004 The most likely path of an energetic charged particle through a uniform medium Phys. Med. Biol. 49 2899–911